Published OnlineFirst June 5, 2013; DOI: 10.1158/1541-7786.MCR-12-0669-T

Molecular Cancer Research

Energy Management by Enhanced Glycolysis in G_1-phase in Human Colon Cancer Cells *In Vitro* and *In Vivo*

Yan Bao, Kuniaki Mukai, Takako Hishiki, et al.

Mol Cancer Res 2013;11:973-985. Published OnlineFirst June 5, 2013.

Cell Cycle and Senescence

Molecular Cancer Research

Energy Management by Enhanced Glycolysis in G_1-phase in Human Colon Cancer Cells *In Vitro* and *In Vivo*

Yan Bao[1], Kuniaki Mukai[1], Takako Hishiki[1,3], Akiko Kubo[1,3], Mitsuyo Ohmura[1], Yuki Sugiura[1], Tomomi Matsuura[1,3], Yoshiko Nagahata[1,3], Noriyo Hayakawa[1,3], Takehiro Yamamoto[1], Ryo Fukuda[1], Hideyuki Saya[2,4], Makoto Suematsu[1,3], and Yoji Andrew Minamishima[1,3]

Abstract

Activation of aerobic glycolysis in cancer cells is well known as the Warburg effect, although its relation to cell-cycle progression remains unknown. In this study, human colon cancer cells were labeled with a cell-cycle phase-dependent fluorescent marker Fucci to distinguish cells in G_1-phase and those in S + G_2/M phases. Fucci-labeled cells served as splenic xenograft transplants in super-immunodeficient NOG mice and exhibited multiple metastases in the livers, frozen sections of which were analyzed by semiquantitative microscopic imaging mass spectrometry. Results showed that cells in G_1-phase exhibited higher concentrations of ATP, NADH, and UDP-N-acetylglucosamine than those in S and G_2–M phases, suggesting accelerated glycolysis in G_1-phase cells *in vivo*. Quantitative determination of metabolites in cells synchronized in S, G_2–M, and G_1 phases suggested that efflux of lactate was elevated significantly in G_1-phase. By contrast, ATP production in G_2–M was highly dependent on mitochondrial respiration, whereas cells in S-phase mostly exhibited an intermediary energy metabolism between G_1 and G_2–M phases. Isogenic cells carrying a p53-null mutation appeared more active in glycolysis throughout the cell cycle than wild-type cells. Thus, as the cell cycle progressed from G_2–M to G_1 phases, the dependency of energy production on glycolysis was increased while the mitochondrial energy production was reciprocally decreased.

Implications: These results shed light on distinct features of the phase-specific phenotypes of metabolic systems in cancer cells. *Mol Cancer Res; 11(9); 973–85. ©2013 AACR.*

Introduction

One of the most significant features of cancer cells is activation of glycolysis even under aerobic conditions. The feature, which has been termed Warburg Effect (1), is observed not only in cancer cells but also in most of proliferating cells (2). An increase in lactate production was found in G_1 phase in HeLa cells (3). Inhibition of glycolysis halted cell-cycle progression in G_1 phase in HeLa cells (4). Enhanced production of lactate with upregulation of glycolytic enzymes was also observed at G_1–S transition in proliferating thymocytes (5). These studies indicate that activity of glycolysis is tightly coupled with cell-cycle progression (6, 7).

On the other hand, previous works have shown that mitochondrial oxidative phosphorylation has key roles in cell-cycle progression (8). Progression of G_1 phase in Jurkat cells was shown to be correlated with activation of respiration (9). Unregulated oxidative phosphorylation induces delayed cell-cycle progression in G_1 phase (10–12). Hyperactivation of mitochondrial functions is critical for entry into S-phase (13). Thus, increasing evidence has suggested that oxidative phosphorylation and glycolysis seem to be coupled with each other and tightly regulated as a function of individual cell-cycle phase during proliferation. However, little information has been available for quantitative data for metabolites *in vivo* or those for metabolic flux of specific metabolic systems involving glycolysis, tricarboxylic acid cycle (TCA) cycle, and high-energy nucleotides in cancer cells or tissues.

In the present study, to investigate coordination between energy metabolism and cell-cycle progression of cancer cells *in vivo*, we have used a human colorectal cancer cell line HCT116 to provide a liver metastasis model in superimmunodeficient NOD/SCID/IL-2Rγ_c^{null} (NOG) mice (14–18). To examine energy metabolism of individual cancer cells in metastatic tumors, we used HCT116 cells labeled

Authors' Affiliations: [1]Department of Biochemistry, and [2]Division of Gene Regulation, Institute for Advanced Medical Research, School of Medicine, Keio University; [3]Japan Science and Technology Agency (JST), Exploratory Research for Advanced Technology (ERATO) Suematsu Gas Biology Project; [4]Japan Science and Technology Agency, Core Research for Evolutional Science and Technology (CREST), Tokyo, Japan

Note: Supplementary data for this article are available at Molecular Cancer Research Online (http://mcr.aacrjournals.org/).

Corresponding Author: Makoto Suematsu, Department of Biochemistry, School of Medicine, Keio University, and Leader, JST ERATO Suematsu Gas Biology Project, 35 Shinanomachi, Shinjuku-ku, Tokyo 160-8582, Japan. Phone: 81-3-5363-3753; Fax: 81-3-5363-3466; E-mail: gasbiology@z6.keio.jp; and Kuniaki Mukai, Department of Biochemistry, School of Medicine, Keio University, 35 Shinanomachi, Shinjuku-ku, Tokyo 160-8582, Japan. Phone: 81-3-5363-3752; Fax: 81-3-5363-3466; E-mail: k-mukai@a3.keio.jp

doi: 10.1158/1541-7786.MCR-12-0669-T

with a cell-cycle phase–dependent fluorescent marker system Fucci (19). With this system, newly developed matrix-assisted laser desorption/ionization imaging mass spectrometry (MALDI-IMS) with high spatial resolution enabled us to reveal spatial distributions and local concentrations of various metabolites in the cancer cells in different cell-cycle phases *in vivo* (20). Application of metabolomic analyses using capillary electrophoresis/electrospray ionization/mass spectrometry (CE/ESI/MS; refs. 21, 22) allows us to determine fluxes of multiple metabolic pathways during cell-cycle progression *in vitro* (20, 23, 24). MALDI-IMS analyses of metastatic tumors have shown that the cancer cells in G_1 phase were more active in glycolysis than those in the other phases. Under synchronized conditions *in vitro*, extracellular secretion of lactate seemed to be accelerated in G_1 phase. In contrast, the cells in G_2–M phase exhibited the highest fraction of mitochondrial oxidative phosphorylation, whereas those in S-phase mostly exhibited an intermediary energy metabolism between G_1 and G_2–M phases, indicating the phase-specific characteristics of energy management of the cancer cells.

Materials and Methods

Cell culture

Human colorectal cancer cell line HCT116 and human embryonic kidney cell line 293T was obtained from the American Type Culture Collection and the Riken Cell Bank, respectively. HCT116 and 293T cells were grown in McCoy's 5A and Dulbecco's modified Eagle medium (DMEM; Gibco), respectively, supplemented with 10% heat-inactivated FBS (Sigma), 200 U/mL penicillin (Gibco), and 200 μg/mL streptomycin (Gibco). HCT116 p53-null cells were a generous gift from Dr. B. Vogelstein (Johns Hopkins Oncology Center, Baltimore, MD), and the absence of p53 was confirmed by Western blot analysis of cell lysates (data not shown). Glucose-free McCoy's 5A medium (Gibco) was used with addition of 3 or 1 g/L of either unlabeled or $^{13}C_6$-labeled D-glucose.

Generation of Fucci-HCT116 cell lines

Viral suspensions for introduction of either mKO2-hCdt1 (30/120) or mAG-hGem(1/110) were prepared with 293T cells as described previously (19, 25, 26). A mixture of the viral suspensions was used to cotransduce HCT116 cells. Cells emitting both red (excitation, 488 nm; emission, 578 nm) and green (excitation, 488 nm; emission, 519 nm) fluorescence were sorted into 96-well plates by a flow cytometer (FACSAria, BD Biosciences). Resulting clones displaying both red (excitation, 543 nm; emission, 560 nm) and green (excitation, 488 nm; emission, 505–550 nm) fluorescence with similar intensities were chosen by using a confocal microscope (LSM510, Carl Zeiss).

Flow cytometry

Nonsynchronizing exponentially growing Fucci-HCT116 cells were incubated with 6 μg/mL Hoechst 33342 (Sigma) at 37°C for 30 minutes. Fluorescence intensity of mKO2, mAG, and Hoechst (excitation, 355 nm; emission, 450–480 nm) was measured using a flow cytometer (FACSAria, BD Biosciences). Synchronized Fucci-HCT116 cells were washed with cold PBS, fixed with 70% ice-cold ethanol, and stained with PBS containing 0.5 μg/mL of 4′,6-diamino-2-phenylindole (DAPI) for 30 minutes. Fluorescence intensity of DAPI was measured using a flow cytometer (EpicsXL, Beckman Coulter).

MALDI-IMS analyses of liver metastases of human colon cancer xenografts *in vivo*

Superimmunodeficient NOG mice (18) were purchased from Central Institute for Experimental Animals. To generate a mouse model for liver metastasis, Fucci-HCT116 cells (1×10^6 cells) were injected into spleen of male mice (25–27 g; 15-weeks-old; $n = 7$). At 10 days after transplantation, liver lobules of the mice fasted for 17 hours were excised under sevoflurane anesthesia and snap-frozen with liquid nitrogen (17). Cryosections (5 μm) of the liver samples were thaw-mounted on indium-tin oxide slides (8–12 ohm/sq; Sigma; ref. 27). Protocols for the above-mentioned experiments were approved by Institutional Committee of Animal Care and Ethics in School of Medicine, Keio University.

Mass spectrometry was conducted in the negative ionization mode by using an atmospheric pressure MALDI-QIT-TOF-MS equipped with a 355 nm Nd:YAG laser (Shimadzu). Fluorescent images of metastatic foci on tissue slices were acquired with a built-in fluorescence microscope and 2 fluorescence mirror units (U-MGFPHO for green fluorescence and U-MWIG3 for red fluorescence; Olympus). Matrix application (27) and acquisition of MALDI imaging data (27) with spatial interval of 20 μm and data processing (27, 28) were carried out as described previously. Measurement points with Fucci-green fluorescence were considered to be cells in S + G_2–M phases. Measurement points with Fucci-red fluorescence proximal to cells in S + G_2–M phases were chosen as cells in G_1 phase because such cells were assumed to be growing actively. To calculate relative concentrations, signal intensities of a metabolite in individual measurement points were normalized by an average value in liver parenchyma of each mouse (Supplementary Fig. S1). Averages of relative concentrations for a metabolite were compared between S + G_2–M phases and G_1 phase.

Cell synchronization and CE/ESI/MS analysis

Cells were synchronized with double thymidine block method. Cells (1.5×10^6 cells per 10 cm dish for metabolomic analysis) were seeded at 24 hours before the first application of thymidine and cultured in the complete medium (containing 1 g/L or 3 g/L glucose) supplemented with 2 mmol/L thymidine for 15 hours, followed by 10-hour incubation with thymidine-free complete medium, and finally incubated for 14 hours with the medium supplemented with 2 mmol/L thymidine. Then, cells were released into the complete medium without thymidine and were collected at 3, 7, and 12 hours after release. Before collection, cells were labeled with $^{13}C_6$-D-glucose

(Isotec) for 5 minutes by exchanging with a glucose-free complete medium supplemented with the labeled glucose at either 1 g/L or 3 g/L.

Cell numbers and protein amounts were determined with additional sets of dishes prepared with the same procedures as described above. Cellular proteins were precipitated by addition of one-tenth volume of 100% (w/v) trichloroacetic acid on ice for 30 minutes followed with an acetone wash. Protein concentrations were determined using the bicinchoninic acid (BCA) method according to the manufacturer's instructions (Micro BCA protein assay, Pierce).

Metabolites were extracted from cells with a solvent composed of methanol, distilled water, and chloroform [methanol:water:chloroform = 1:0.5:1 (v/v/v)]. After centrifugation at 20,000 *g* at 4°C for 15 minutes, the supernatants were filtered through 5 kDa cut-off filter (Millipore). Metabolites including those that had at least one ^{13}C atom in the filtrate were analyzed by using an Agilent CE Capillary Electrophoresis System equipped with an Agilent 1100 series MSD mass spectrometer, as described previously (24). Labeled metabolites containing at least one ^{13}C atom in a molecule were collectively indicated as ^{13}C-labeled forms. Total molar amounts of metabolites in each of different metabolic pathways were sums of measured values for the following metabolites: for glycolysis, glucose-1-phosphate, glucose-6-phosphate+fructose-6-phosphate, fructose-1,6-diphosphate, dihydroxyacetonephosphate, DL-glyceraldehyde-3-phosphate, 1,3-diphosphoglycerate, 2-phosphoglycerate+3-phosphoglycerate, phosphoenolpyruvate, pyruvate, and lactate; for TCA cycle, acetyl-CoA, citrate, *cis*-aconitate, isocitrate, 2-oxoglutarate, succinyl-CoA, succinate, fumarate, and malate; for pentose phosphate pathway (PPP), gluconate, 6-phosphogluconate, ribulose-5-phosphate, xylulose-5-phosphate+ribose-5-phosphate, D-sedoheptulose-7-phosphate, and erythrose-4-phosphate. Amount of oxaloacetate was not included in the data because it was unable to be measured by CE/ESI/MS.

Lactate efflux assay

Concentrations of extracellular lactate were measured using a lactate dehydrogenase-based kit (F-kit L-Lactate, Roche Diagnostics). Amounts of lactate accumulated in media (0.2 mL) were assayed at 1, 2.75, 5, 6.75, 9, and 12 hours after releasing. Rates of lactate efflux were determined by measuring lactate amounts in media after 30 minutes from exchanging with fresh media at time points of 2.75, 6.75, and 12 hours.

Assays for reduced and oxidized forms of glutathione (GSH and GSSG)

Cells were collected in a solution containing 5% metaphosphoric acid and 100 μmol/L diethylenetriamine pentaacetate (Sigma). After centrifugation at 20,000 × *g* at 4°C for 10 minutes, the supernatant were filtered through 0.45 μm filter (Millipore) for assays. GSH and GSSG were detected with an HPLC-coulometric electrode array detector (Coularray Detector, model 540 with 8 channels; ESA Bioscience ref. 29).

Assays for activities of glycolytic enzymes and Western blot analysis

Cells were collected by scraping and suspended in extraction buffer containing 50 mmol/L Tris-acetate, pH 7.8, 10 mmol/L dithiothreitol, 1 mmol/L EDTA-Na, pH 8.0, and a cocktail of protease inhibitors (Roche). After sonication for 4 separate periods of 30 seconds at 200 W on ice, the suspensions were centrifuged at 20,000 × *g* for 10 minutes, and the supernatants were saved. Activities of phosphofructokinase (PFK), glyceraldehyde-3-phosphate dehydrogenase (GAPDH), and pyruvate kinase (PK) were determined by monitoring changes in absorbance at 340 nm as described previously (5, 30, 31).

Cells were lysed with 8 mol/L urea containing 10 mmol/L Tris-HCl (pH 7.4), 1 mmol/L EDTA. Protein extract (50 μg) were resolved by SDS-PAGE and transferred onto polyvinylidene difluoride membranes (GE Healthcare). Membranes were blocked with PBS-based blocking buffer (#927–40000; LI-COR, Lincoln) and probed with the following primary antibodies: Rabbit anti-PFKP (#AP8135b; Abgent), mouse anti-PFKFB3 (#H00005209-M08; Abnova), and mouse anti-Vinculin (#V9131; Sigma-Aldrich). Bound antibodies were detected with secondary antibodies [IR dye-conjugated goat anti-rabbit IgG (#926–32211; LI-COR) for PFKP, sheep anti-mouse IgG (#NA9310; GE Healthcare, UK) for PFKFB3, and infrared (IR) dye-conjugated goat anti-mouse IgG (#926–32210; LI-COR) for Vinculin]. Signals were visualized with Immobilon Western chemiluminescent HRP substrate (Millipore) for PFKP or directly imaged for PFKP and Vinculin with infrared/chemiluminescent dual imaging system (Odyssey FC; LI_COR).

Mitochondrial DNA copy number

Total DNA was isolated from cells by using a DNeasy DNA extraction kit (Qiagen) and conventional phenol–chloroform extraction. The relative copy number of cytochrome *b* gene to RPL13A gene was determined by quantitative real-time PCR (7300 real-time PCR system, Applied Biosystems). Sequences of the primers were described previously (32).

Determination of reactive oxygen species

Fucci-HCT116 cells cultured with 96-well plates were loaded with medium containing 5 μmol/L CellROX Deep Red reagent (Invitrogen) and incubated at 37°C for 1 hour. The near-infrared fluorescence of CellROX Deep Red (excitation, 640 nm; emission, 670 nm) was detected using a fluorescence plate reader (Synergy 4, Biotek).

Mitochondrial inner membrane potential

HCT116 cells were seeded at 1×10^5 cells in a 35 mm dish with 12 mm glass base (Iwaki) and synchronized as described above. After release, cells were cultured with 17 nmol/L tetramethylrhodamine ethylester (TMRE, Invitrogen) and 6 μg/mL Hoechst 33342 for 20 minutes in the dark. Fluorescence of TRME (excitation, 568 nm; emission, 590–630 nm) and Hoechst 33342 (excitation,

325–350 nm; emission, 400–416 nm) was detected by using a laser scanning confocal microscope (Olympus, FV10i).

Extracellular acidification rate

HCT116 and HCT116 p53-null cells were seeded at 2×10^4 cells per well in 24-well plates (Seahorse Bioscience), and synchronized with the double thymidine method. After releasing for 2.5, 6.5, and 11.5 hours, the cells were equilibrated with DMEM without bicarbonate (Seahorse Bioscience) in a non-CO_2 incubator at 37°C for 30 minutes. Extracellular acidification rate (ECAR) were recorded simultaneously by using a Seahorse Bioscience XF24 plate reader at 3, 7, and 12 hours after releasing, according to the manufacturer's instruction (8).

Statistical analysis

Data were analyzed by using Statcel3 software package (OMS Publishing Inc.). ANOVA was used to evaluate differences in data among S, G_2–M, and G_1 phases *in vitro*. Paired Student *t* test was used to examine differences in data between S + G_2–M and G_1 phases *in vivo*. Values are expressed as mean ± SEM. $P < 0.05$ was considered statistically significant.

Results

Fucci-HCT116 cells in metastatic foci with higher ATP levels in G_1 phase than in S and G_2–M phases

To study how energy metabolism is coordinated with cell-cycle progression in cancer cells, we used human colon cancer HCT116 cells and their stable transfectants, Fucci-HCT116 cells, which were generated by introduction of the Fucci system into the parental cells. Flow cytometry of growing Fucci-HCT116 cells for expression of the Fucci markers showed red-, yellow-, and green-emitting populations. DNA contents of the cells stained with Hoechst 33342 indicated that cells in G_1 phase were red; cells in S-phase were yellow or green; cells in G_2–M phase were green (Fig. 1A). The introduction of the Fucci markers did not change the populations in G_1, S, and G_2–M phases from those in parental HCT116 cells (data not shown). To observe changes in metabolism in cell-cycle progression *in vivo*, we used a NOG mouse model for liver metastasis of Fucci-HCT116 cells. With MALDI-IMS, relative concentrations of metabolites, all of which we have described as successful quantitation (27), in tumor cells were determined. Measurement points corresponding to tumor cells with Fucci-green fluorescence (S + G_2–M phases) and those with Fucci-red fluorescence (G_1 phase) were assigned precisely using built-in fluorescence image capturing system (Fig. 1B). It was notable that the percentages of cells in S + G_2–M phases *in vivo* were smaller than those under culture conditions (Fig. 1B, Supplementary Table S1, and see the following sections), suggesting that proliferation of cells in the metastatic foci was less active than those under culture conditions. Ion density images from MALDI-IMS displayed *in situ* distributions of 10 metabolites involved in energy and redox metabolism (Fig. 1C).

Relative concentrations, which were normalized by values of parenchyma in each mouse, of ATP, UTP, NADH, UDP-*N*-acetylglucosamine (UDP-GlcNAc), and GSSG in cells in G_1 phase were found to be significantly greater than those in S + G_2–M phases in the foci (Fig. 1D and Supplementary Fig. S1). On the other hand, relative concentrations of ADP, AMP, UDP, UMP, and GSH did not differ significantly between S + G_2–M and G_1 phases (Fig. 1D). The results that the concentrations of nucleotide triphosphates and NADH were higher in G_1 phase cells than in S + G_2–M phase cells suggested that the cells exhibited cell-cycle phase-dependent energy metabolism, possibly executing glycolysis more actively in G_1 phase than in the other phases.

Synchronization of Fucci-HCT116 cells in G_1, S, and G_2–M phases

As Fucci-HCT116 cells in S and G_2–M phases both emitted green fluorescence, they could not be distinguished from each other by the fluorescence. To understand cell-cycle–dependent changes in energy metabolism clearly, we used synchronized cells prepared *in vitro* with the double thymidine block method (Fig. 2A–C). At 3, 7, and 12 hours after release from the thymidine treatment, cells were harvested and DNA contents of the cells were analyzed by flow cytometry. The results indicated that the cells collected at 3 hours were almost in S-phase (75%); those at 7 hours were in G_2–M phase (85%); and those at 12 hours were in G_1 phase (88%; Fig. 2B). Fluorescence microscopy of the synchronized Fucci-HCT116 cells showed that more than 70% of cells emitted green or yellow fluorescence at 3 and 7 hours after the release; and 89% of the cells emitted red fluorescence at 12 hours after the release (Fig. 2C). Thus, the detected fluorescence introduced by Fucci system was consistent with the classical methodology.

For general characterization of Fucci-HCT116 cells in different cell-cycle phases, we examined cell numbers, cell volumes, and protein amounts of the synchronized populations, which were derived from the same numbers of cells inoculated before thymidine treatment. As shown, the cell numbers unchanged from S to G_2–M phase, and then increased twice in G_1 phase (Fig. 2D). The volumes of individual cells reached the maximum in G_2–M phase and showed a dramatic decrease in G_1 phase (Fig. 2E and F). The total protein amounts of collected cells in different phases tended to increase gradually (Fig. 2G). The protein amounts per cell decreased in G_1 phase by 36% from that in G_2–M phase (Fig. 2H), whereas the protein amounts per cell volume in G_1 phase increased by 58% from those in G_2–M phase (Fig. 2I). These observations through cell-cycle progression may help to understand changes in the energy metabolism in the following sections.

Higher ATP levels in G_1 phase than in S and G_2–M phases of HCT116 cells *in vitro*

To know whether *in vitro* cells exhibited cell-cycle phase–dependent metabolic changes similar to those seen *in vivo*, we used synchronized cells in S, G_2–M, and G_1 phases *in vitro* and determined cellular concentrations of the same set

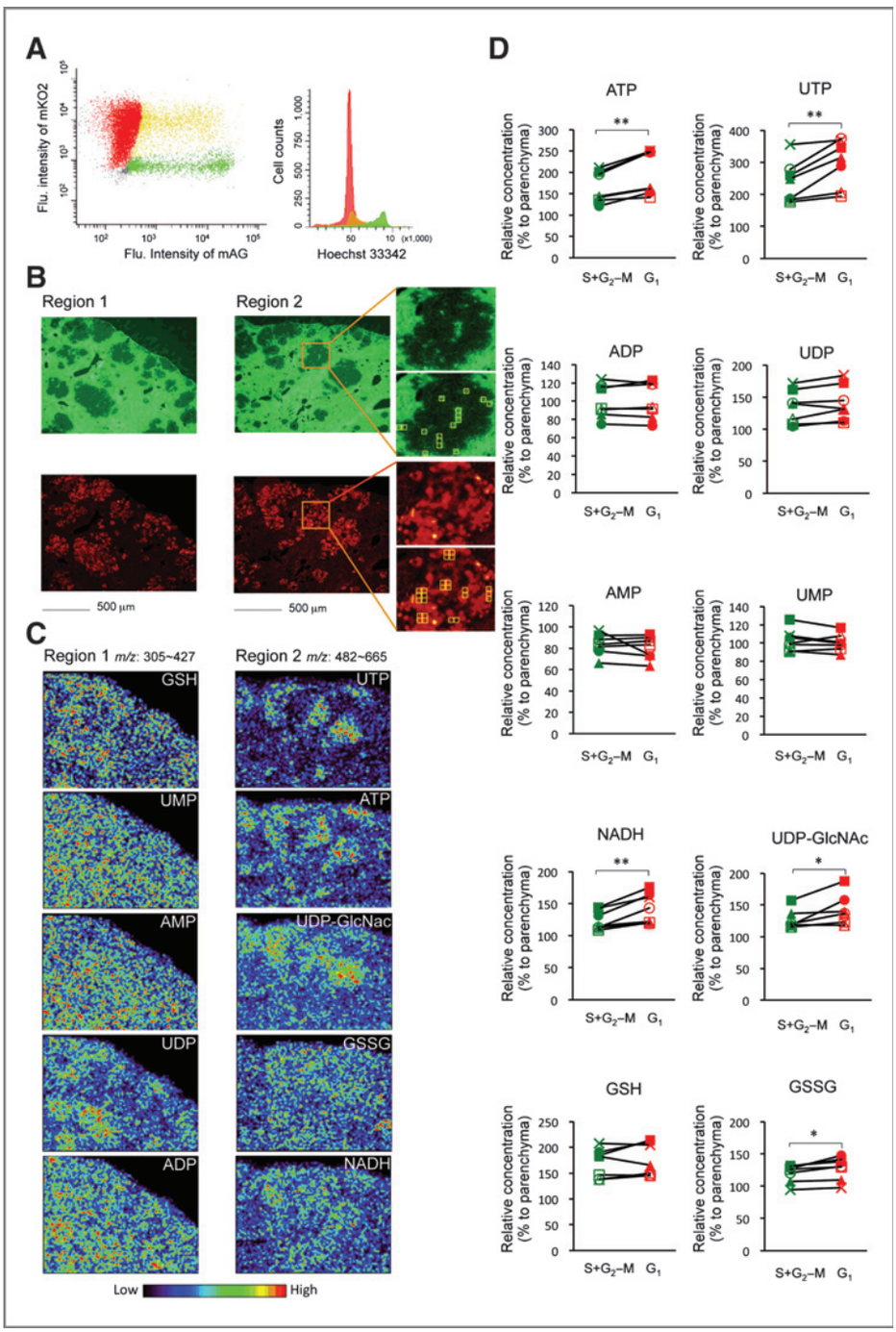

Figure 1. Fucci-HCT116 cells in metastatic foci with higher ATP levels in G_1 phase than in S and G_2–M phases. A, exponentially proliferating Fucci-HCT116 cells were stained with Hoechst 33342 (6 μg/mL) for 90 minutes. Left, cell populations with mKO2 (red), mAG (green), and both mKO2 and mAG (yellow). Right, DNA contents of the different cell populations shown in left with red, green, or yellow. B–D, liver sections (5 μm) from 7 NOG-mice carrying metastatic foci consisting of Fucci-HCT116 cells were examined for relative concentrations of metabolites. Images of liver sections from a NOG mouse (mouse number 3) are shown in B and C. B, green (Fucci-green and liver parenchymal autofluorescence) and red (Fucci-red) fluorescence images of sections are displayed separately. Areas framed with orange lines are enlarged to show cells in S + G_2–M phases with green fluorescence or cells in G_1 phase with red fluorescence (top) and measurement points as small squares (bottom). Two representative sets were shown: left (Region 1), data with *m/z* ranging from 305 to 427 for GSH (*m/z* 306.07), UMP (323.02), AMP (346.05), UDP (403.00), and ADP (426.02); right (Region 2), data with *m/z* ranging from 482 to 665 for UTP (*m/z* 482.93), ATP (505.98), UDP-GlcNAc (606.06), GSSG (611.14), and NADH (664.09). C, ion density images of metabolites in the regions shown in (B) are displayed. D, relative concentrations to parenchyma (normalized by averages from liver parenchyma) of metabolites in S + G_2–M phases and in G_1 phase were calculated and statistically examined with Student-paired *t* test. $n = 7$ (mouse numbers 1–7 are indicated, respectively, with closed circles, closed squares, closed triangles, crosses, open circles, open squares, and open triangles). *, $P < 0.05$; **, $P < 0.01$. See also Supplementary Table S1 for percentages of green- and red-fluorescent nuclei in foci of 7 mice, Supplementary Table S2 for numbers of measurement points from the foci, and Supplementary Fig. S1 for frequency distributions of relative MALDI-IMS signal intensities of measurement points to liver parenchyma in mouse number 3.

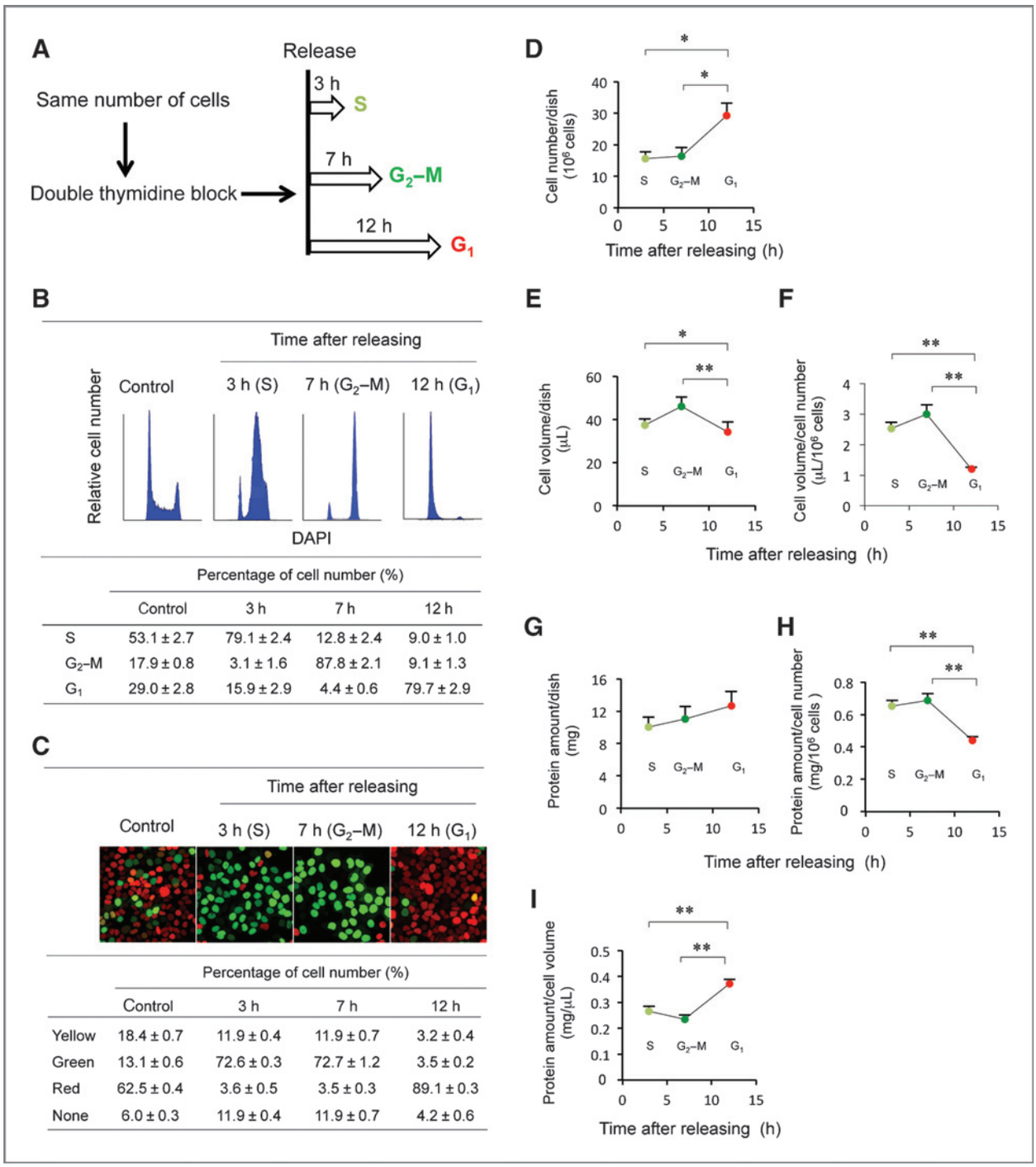

Percentage of cell number (%)				
	Control	3 h	7 h	12 h
S	53.1 ± 2.7	79.1 ± 2.4	12.8 ± 2.4	9.0 ± 1.0
G_2–M	17.9 ± 0.8	3.1 ± 1.6	87.8 ± 2.1	9.1 ± 1.3
G_1	29.0 ± 2.8	15.9 ± 2.9	4.4 ± 0.6	79.7 ± 2.9

Percentage of cell number (%)				
	Control	3 h	7 h	12 h
Yellow	18.4 ± 0.7	11.9 ± 0.4	11.9 ± 0.7	3.2 ± 0.4
Green	13.1 ± 0.6	72.6 ± 0.3	72.7 ± 1.2	3.5 ± 0.2
Red	62.5 ± 0.4	3.6 ± 0.5	3.5 ± 0.3	89.1 ± 0.3
None	6.0 ± 0.3	11.9 ± 0.4	11.9 ± 0.7	4.2 ± 0.6

Figure 2. Synchronization of Fucci-HCT116 cells in S, G_2–M, and G_1 phases. A, scheme of preparation of synchronized cells. The same numbers of cells were plated on different dishes and treated with double thymidine block as described in Materials and Methods. Synchronized cells were collected from the dishes at 3 (S phase), 7 (G_2-M phase), and 12 (G_1 phase) hours after released from excess thymidine. B, flow cytometry for DNA contents of synchronized cells. Cells were fixed and stained with DAPI. Nonsynchronized Fucci-HCT116 cells were used as a control. Percentages of cells in S, G_2–M, and G_1 phases are shown. $n = 3$, mean values ± SEM. C, fluorescence of living Fucci-HCT116 after release was examined using confocal fluorescence microscopy. Percentages of nuclei with red, green, yellow, and no fluorescence are shown. $n = 4$, mean values ± SEM. D–I, Fucci-HCT116 cells (6×10^6 cells/15-cm dish) were seeded and synchronized. Cells collected at 3, 7, and 12 hours after release were examined for (D) cell numbers per dish; (E) total volumes of cells per dish which were calculated from mean values of cell diameters in specific cell-cycle phases and cell numbers; (F) cell volumes per 10^6 cells; (G) protein amounts per dish; (H) protein amounts per 10^6 cells; (I) protein amounts per milliliter of cell volume. $n = 6$, mean values ± SEM. *, $P < 0.05$; **, $P < 0.01$.

of the metabolites as examined *in vivo* except for UDP-GlcNAc. Under conditions in culture, ATP concentration in G_1 phase was significantly higher than the other phases, whereas calculated values for energy charge did not change among the 3 phases (Fig. 3A). GSH and GSSG concentrations were both greater in G_1 phase than in the other phases significantly (Fig. 3B).

Next, to obtain comprehensive information on changes in energy metabolism in cell-cycle progression, we measured various metabolites in glycolysis, TCA cycle, and PPP in S, G_2–M, and G_1 phases by using CE/ESI/MS. The samples were prepared from synchronized cells which were derived from same numbers of inoculated cells. Molar amounts were used for comparison of the data among the cell-cycle phases. For analyses of metabolic flux, cells were labeled with medium containing $^{13}C_6$-labeled glucose for 5 minutes before extraction. Amounts of lactate, pyruvate, and total amounts of glycolytic metabolites did not change in the cell-cycle progression (Fig. 4A–C). It should be noted that cellular amounts of lactate were predominant among the metabolites of the 3 pathways through the cell-cycle phases. The cellular amounts of the metabolites in each of the 3 pathways were almost unchanged in the cell-cycle progress (Fig. 4C). Amounts of ^{13}C-labeled metabolites (at least one carbon atom was labeled) showed that the metabolites in glycolytic pathway were labeled more quickly than those in TCA cycle and in PPP (data not shown) in the cell-cycle progression (Fig. 4D and E).

As HCT116 cells whose data described above carry wild-type p53, a key regulator of glycolysis, we also collected data from isogenic HCT116 cells with p53-null mutation and from wild-type cells cultured at a euglycemic level (1 g/L).

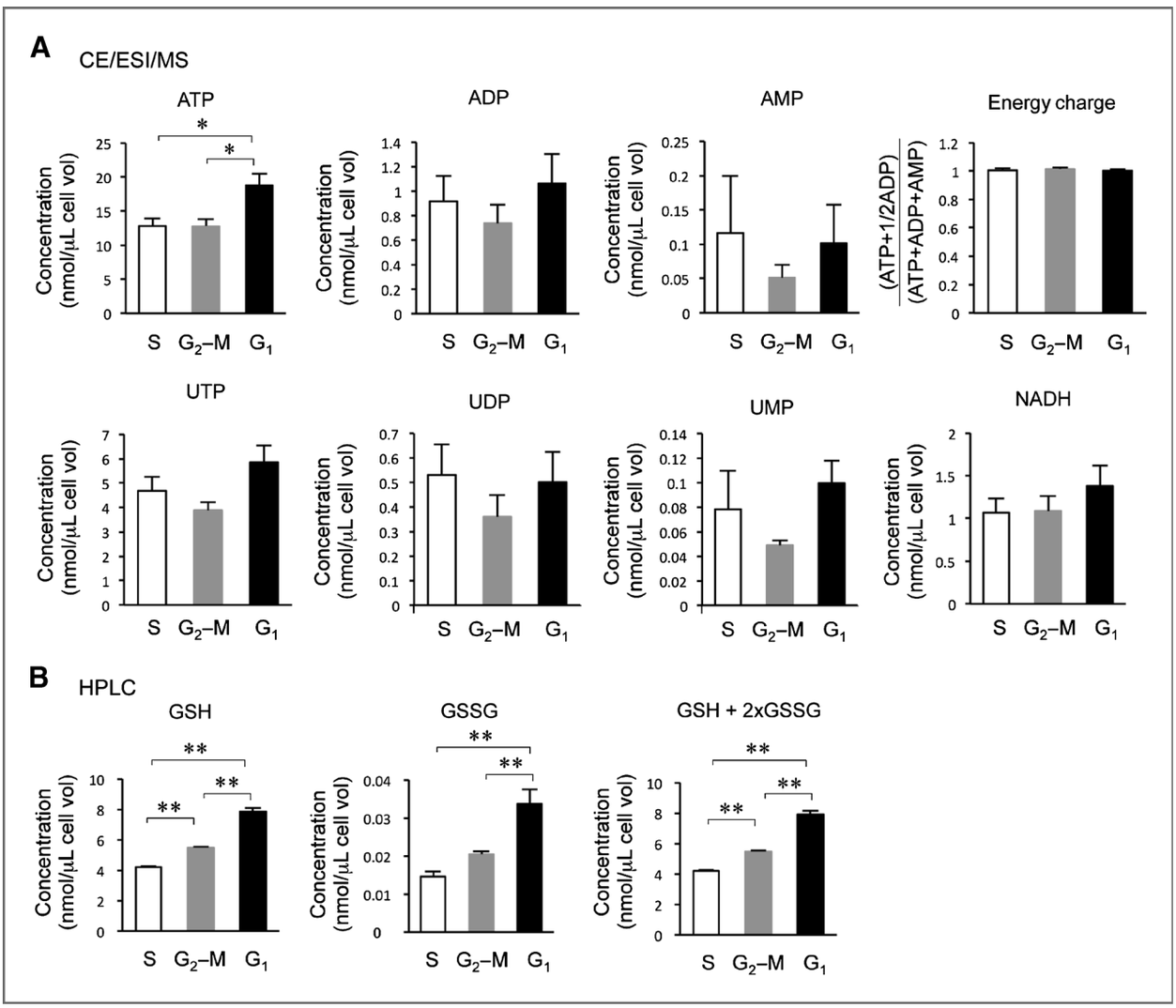

Figure 3. ATP concentration arises in G_1 phase of HCT116 cells *in vitro*. Cellular concentrations of metabolites in synchronized cells in S, G_2–M, and G_1 phases were determined using (A) CE/ESI/MS ($n = 6$) and (B) HPLC-coulometric electronic array detector ($n = 5$). Values for energy charge were calculated from the concentrations of adenine nucleotides. Cells collected in the different phases were derived from the same numbers of cells. Mean values ± SEM. *, $P < 0.05$; **, $P < 0.01$.

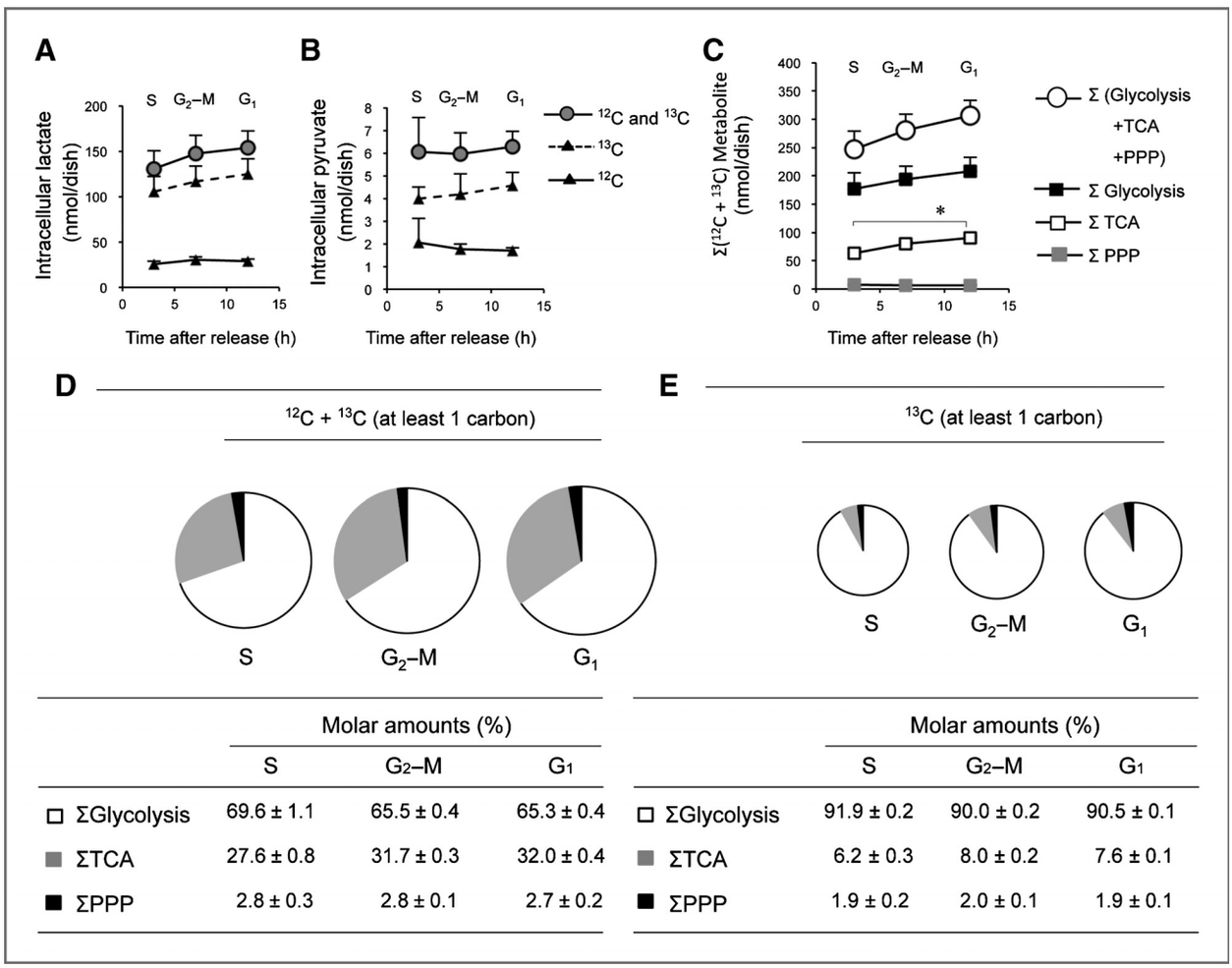

	Molar amounts (%)		
	S	G2–M	G1
ΣGlycolysis	69.6 ± 1.1	65.5 ± 0.4	65.3 ± 0.4
ΣTCA	27.6 ± 0.8	31.7 ± 0.3	32.0 ± 0.4
ΣPPP	2.8 ± 0.3	2.8 ± 0.1	2.7 ± 0.2

	Molar amounts (%)		
	S	G2–M	G1
ΣGlycolysis	91.9 ± 0.2	90.0 ± 0.2	90.5 ± 0.1
ΣTCA	6.2 ± 0.3	8.0 ± 0.2	7.6 ± 0.1
ΣPPP	1.9 ± 0.2	2.0 ± 0.1	1.9 ± 0.1

Figure 4. Glycolysis dominates in energy metabolism throughout cell-cycle progression *in vitro*. Amounts of metabolites in cells synchronized in S, G_2–M, and G_1 phases were determined by using CE/ESI/MS. Cells collected in the different phases were derived from the same numbers of cells plated on dishes. Before collection, cells were labeled with $^{13}C_6$-D-glucose for 5 minutes. A, lactate; B, pyruvate. $n = 3$, mean values ± SEM. Molar amounts of unlabeled metabolites/dish (^{12}C, triangles with solid line), ^{13}C-labeled (at least one carbon atom is labeled) metabolites/dish (^{13}C, triangles with dashed line), and unlabeled plus ^{13}C-labeled metabolites/dish (^{12}C and ^{13}C, circles) are shown. C, total amounts of unlabeled plus ^{13}C-labeled metabolites/dish in different metabolic pathways: glycolysis (closed squares): TCA cycle (open squares); PPP (gray squares); sum of the 3 pathways (open circles). $n = 3$, mean values ± SEM. D and E, percentages of molar amount of metabolites in the 3 pathways [glycolysis (white); TCA cycle (gray); PPP (black)] are shown in each pie chart, and areas are proportional to molar amounts. $n = 6$, mean values ± SEM. D, ^{13}C-labeled plus unlabeled metabolites. E, ^{13}C-labeled metabolites. *, $P < 0.05$; **, $P < 0.01$.

The same experimental protocols could be applied to the 2 sets of conditions as judged by DNA content (Supplementary Fig. S2) and could give similar results on cellular amounts of metabolites as those obtained with wild-type cells at 3 g/L glucose (Supplementary Fig. S3–S5).

Glycolysis is accelerated in G_1 phase to greater extents than the other phases

Because lactate was the predominant metabolite which is released from cells as a result of glycolysis, we next examined amounts of extracellular lactate in the progress of cell cycle. When accumulation of extracellular lactate after wash-out of thymidine was examined, wild-type cells under 3 g/L glucose showed gradual increases in lactate levels with a small decrease in slope at G_2–M phase (Fig. 5A, dots with solid line). Measurements of release rates of lactate by replacing with fresh media indicated that the observed rate in G_1 phase was higher than S and G_2–M phases with statistical significances (Fig. 5B, dots with solid line). These results suggest that glycolysis is markedly accelerated in G_1 phase to greater extents than the other phases.

Extracellular lactate was being accumulated in wild-type cells at a euglycemic level with a similar manner, except for a marked halt in G_2–M phase, as seen under 3 g/L glucose condition (Fig. 5A, gray squares with gray line). On the other hand, extracellular lactate in p53-null cells at 3 g/L glucose was being accumulated with almost linear pattern throughout the cell-cycle progression (Fig. 5A, triangles with dashed line). These observations were consistent with releasing rates of lactate (Fig. 5B and Supplementary Fig. S6).

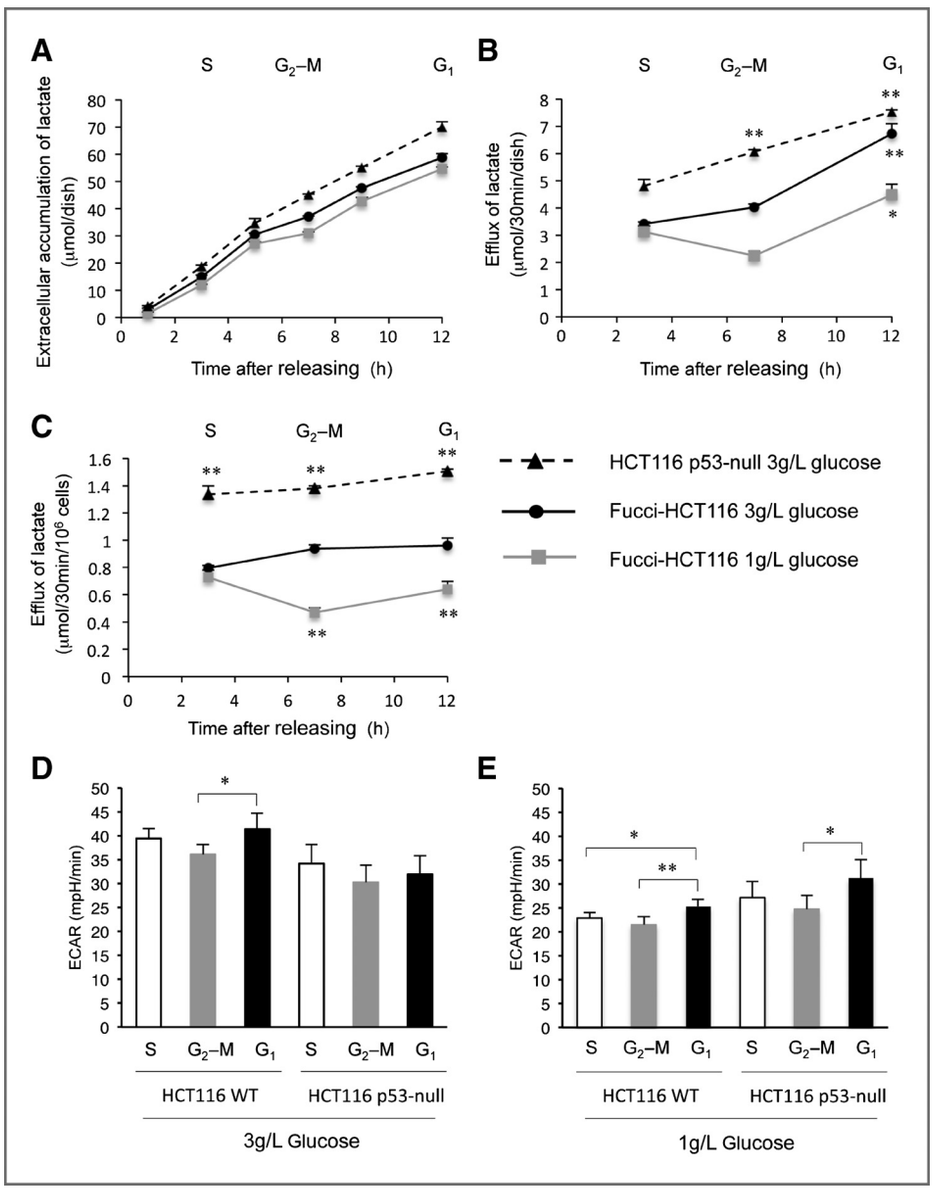

Figure 5. Glycolysis is accelerated in G_1 phase to greater extents than in other phases. A, amounts of lactate accumulated in media (0.2 mL) were assayed at 1, 2.75, 5, 6.75, 9, and 12 hours after releasing. Note that acuumulation rate was temporary decreased at G_2–M phase in HCT116 WT cells. B, rates of lactate efflux were examined by measuring lactate amounts in media after 30 minutes from exchanging with fresh media at time points of 2.75, 6.75, and 12 hours. Statistical significance was examined for differences in data between 2 successive time points. C, rates of lactate efflux were normalized by cell numbers. Statistical significance was examined for differences in data of either wild-type cells (1 g/L glucose) or p53-null cells (3 g/L glucose) from wild-type cells (3 g/L glucose) at individual time points. $n = 3$, mean values ± SEM. *, $P < 0.05$; **, $P < 0.01$. D and E, ECARs were real-time measured using Seahorse XF24 Analyzer in HCT116 WT and HCT116 p53-null cells in indicated cell-cycle phases (S, G_2–M and G_1) as described in Materials and Methods section. $n = 6$, mean values ± SEM. *, $P < 0.05$; **, $P < 0.01$.

Furthermore, when the releasing rates, which were normalized by cell numbers, were compared among the three sets of the data, p53-null mutation might activate glycolysis (Fig. 5C).

Although intracellular lactate level was not significantly changed between genotypes or culture conditions during cell-cycle progression (Fig. 4A), ECAR, marker for lactate production rate, was significantly increased in G_1 phase in HCT116 WT cells cultured with both 1 g/L and 3 g/L of glucose and HCT116 p53-null cells with 1 g/L glucose (Fig. 5D and E). We have also checked the expression of several monocarboxylate transporters (MCT) as extracellular lactate level depends on both import and export rate of lactate. mRNA expression levels of MCT1 and MCT4 did not change significantly throughout cell-cycle progression, suggesting that lactate efflux might not depend on expression level of lactate transporters (Supplementary Fig. S7).

Glycolytic enzyme activities may explain in part changes in glycolytic rates in cell-cycle progression

We measured activities of a certain set of glycolytic enzymes to investigate possible causes of the changes in glycolytic activities throughout cell-cycle phases. Soluble proteins were extracted from cells in S, G_2–M, and G_1 phases, which were derived from the same number of cells, and enzymatic activities of PFK, GAPDH, and PK were examined. The activities of the three enzymes in S, G_2–M, and G_1 phases gave similar patterns to one another; for all of the three enzymes, the activities in S and G_1 phases were similar to each other and higher than those in G_2–M phase (Fig. 6A–C). These results may explain in part changes in

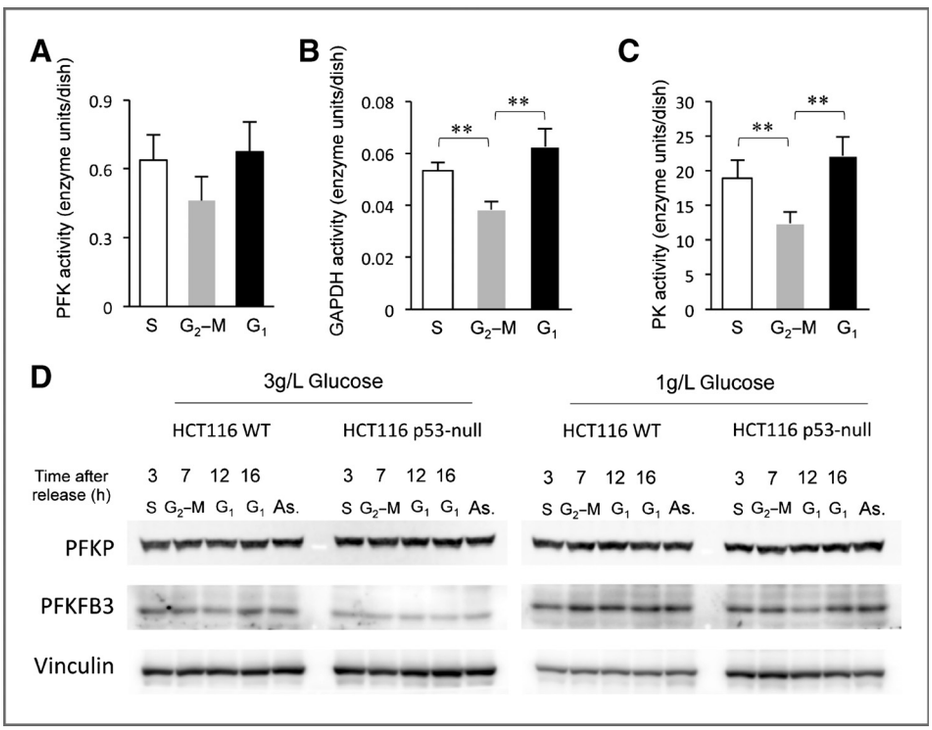

Figure 6. Differences in activities of glycolytic enzymes among cell-cycle phases do not necessarily explain cell-cycle phase–dependent changes in energy metabolism. Soluble extracts from cells in S phase (open bars), G_2–M phase (gray bars), and G_1 phase (closed bars) were assayed for (A) PFK, (B) GAPDH, and (C) PK activities as described in Materials and Methods. Cells collected in the different phases were derived from the same numbers of cells. Enzymatic activities are shown as enzyme units per dish. $n = 5$, mean values ± SEM. **, $P < 0.01$. D, Western blot analysis of PFKP and PFKFB3. HCT116 WT and p53-null cells were released from thymidine block and cell extracts were prepared 3, 7, 12 and 16 hours after release. Vinculin was also probed as a loading control. "As." indicates protein extracts from asynchronized cells. Glucose concentration in culture media is also indicated.

glycolytic rates (Fig. 5B, solid line) and ECAR (Fig. 5D, wild-type cells in 3 g/L glucose) in cell-cycle progression.

We further examined protein levels of PFKP, a subunit of PFK, and PFKFB3 (6-phosphofructo-2-kinase/fructose-2,6-biphosphatase 3) in the cell-cycle progression of the wild-type cells and p53-null cells in both high (3 g/L) and low (1 g/L) glucose concentrations. Western blot analyses indicated that the levels of the proteins in the 2 types of cells did not significantly alter in the cell-cycle progression under both glucose concentrations (Fig. 6D). The enzyme amounts did not necessarily account for the changes in glycolytic activity in the cell-cycle progression.

Mitochondrial oxidative phosphorylation is activated in G_2–M phase

We subsequently examined how mitochondrial oxidative phosphorylation activity changed in the cell-cycle progression. Measurements of oligomycin-sensitive ATP production showed that percentages of mitochondrial production of ATP were the highest (41%) in G_2–M phase and the lowest (9%) in G_1 phase (Fig. 7A) without apparent changing in mitochondrial DNA copy number over genomic DNA (Fig. 7B). Thus, dependence of ATP synthesis on mitochondria was higher in G_2–M phase than in G_1 phase. The levels of cellular ROS, a by-product from the electron transfer, were the highest in G_2–M phase among the cell-cycle phases (Fig. 7C), suggesting the most active electron transfer activity in the phase. Inner mitochondrial membrane potential in G_1 phase, however, was kept being 1.5-fold higher than in S and G_2–M phases, implying that the potential was not so efficiently consumed to produce ATP in G_1 phase as in S and G_2–M phases (Fig. 7D).

Discussion

In the present study, we deepened the understanding of energy metabolism of cancer cells. This was carried out by measuring metabolites of synchronized cells *in vitro* in different cell-cycle phases using mass spectrometry. We showed that glycolysis was dominant in the energy metabolism throughout the cell-cycle progression with an enhancement in G_1 phase, whereas mitochondrial oxidative phosphorylation was reciprocally activated in S and further in G_2–M phases. Consequently, these results together with the current observations *in vivo* provided for the first time substantial evidence for the cell-cycle–dependent patterns in energy metabolism of cancer cells *in vitro* and *in vivo.*

This study added a new viewpoint of cell-cycle phases to the energy metabolism including the Warburg effect. Previous studies focusing on a segment in energy-acquiring metabolisms or specific metabolites have shown cyclic changes in oxygen consumption (33), concentrations of glycolytic intermediates (34), ATP (35), and lactate (3) in proliferating cells. Since these studies have not examined the whole pathways of energy metabolism in different cell-cycle phases, they did not depict an overall picture of the energy metabolism throughout cell proliferation processes. In contrast, our study dissected metabolic systems for energy management into glycolysis, oxidative phosphorylation, and PPP and used *in vitro* cancer cells synchronized in S, G_2–M, and G_1 phases.

Several lines of evidence indicate cell-cycle phase–dependent changes in energy metabolism in culture where sufficient amounts of glucose and oxygen are available. First, the energy production in G_1 phase highly depends on glycolysis

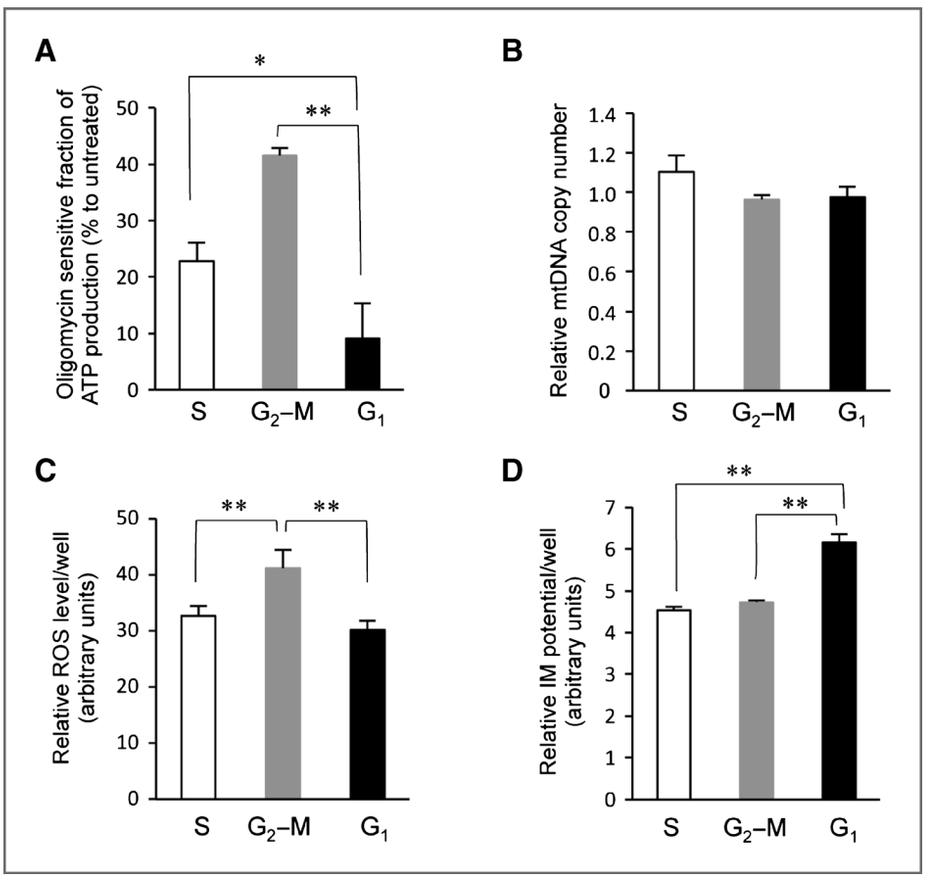

Figure 7. Mitochondrial oxidative phosphorylation is activated in G_2–M phase. HCT116 cells synchronized in different cell-cycle phases were derived from the same numbers of cells in each of the following experiments. A, fraction of mitochondrial production of ATP. Before determination, cells were incubated in the presence or absence of oligomycin (20 μg/mL) for 1 hour. ATP production in each phase was measured with the luciferin–luciferase reaction. $n = 7$, mean values ± SEM. B, relative numbers of mitochondrial DNA to nuclear DNA. Copy numbers of a mitochondrial gene (cytochrome *b*) and a nuclear gene (RPL13A) in cells in different phases were determined by quantitative real-time PCR. Ratios relative to the value obtained from G_1 phase were shown. $n = 3$, mean values ± SEM. C, intracellular ROS levels. ROS levels in cells in S, G_2–M, and G_1 phases were measured with a fluorescent dye, CellROX Deep Red. Cells were stained with 5 μmol/L CellROX Deep Red in complete medium for 1 hour. Intensities of the oxidized dye per well were shown. $n = 10$, mean values ± SEM. D, relative mitochondrial inner membrane (IM) potential. Cells were stained with 17 nmol/L TMRE in complete medium for 20 minutes. Intensities of TMRE fluorescence per well are shown. $n = 5$, mean values ± SEM.

with only a small fraction of mitochondrial respiration. Data of the metabolite measurements, especially extracellular lactate, suggested that the glycolytic activity was the most active in G_1 phase. Inversely, the mitochondrial contribution to ATP production was also minimal in G_1 phase. Thus, Warburg effect was seen most evidently in the G_1-phase cancer cells. Second, the G_2–M phase exhibited the highest dependence of energy production on mitochondrial respiration. The fraction of mitochondrial ATP production were the highest values in G_2–M phase together with the greatest levels of ROS production presumably because of the active electron-transferring activities. Third, the energy metabolism in S-phase mostly exhibited an intermediary between G_1 and G_2–M phases. Thus, as the cell cycle progressed from G_2–M to G_1 phases, the dependence of energy production on glycolysis in the cancer cells was drastically increased, whereas mitochondrial contribution was reciprocally decreased. As discussed later, since energization in G_1 phase is a requisite for passing through the metabolic checkpoint (10, 36, 37), the enhancement of glycolysis in G_1 phase may energize the cells and avoid G_1 arrest.

The combination of the Fucci system, the mouse model for metastasis, and the MALDI-IMS in this study cast new light on *in vivo* studies on energy metabolism of solid cancer. In fact, the significant increase in concentrations of ATP and UTP in G_1 phase was greater than in S and G_2–M phases *in vivo*. As UDP-GlcNAc levels are elevated in parallel with glucose use (38), the current observation showing the higher level of UDP-GlcNAc in G_1 phase *in vivo* suggests a possible accelerated glucose uptake in the phase. When the concentrations of metabolites were compared between *in vitro* and *in vivo*, there were some discrepancy, i.e., cellular amounts of GSH were greater in G_1 than in G_2–M phase *in vitro*, whereas they did not statistically differ *in vivo*. The discrepancy between *in vitro* and *in vivo* might result from different conditions such as supplies of oxygen and nutrients. In

addition, different from the synchronized cells *in vitro*, green cells in S phase and those in G_2–M phase were indistinguishable *in vivo*, and red cells *in vivo* should consist of cells at various positions in G_1 phase. Nevertheless, the *in vivo* measurements showed greater concentrations of the nucleotide triphosphates of cancer cells in G_1 phase, possibly due to further activation of glycolysis, as compared with those in S and G_2–M phases.

The enhancement of glycolysis in G_1 phase is a distinct feature that may be exploited for control of cell-cycle progression in cancer cells. Between G_1 and S phases, there is a metabolic checkpoint that determines whether cells undergo G_1 arrest or proliferate (36, 37). AMP-activated protein kinase (AMPK) serves as a sensor for low energy, and its activation inhibits cell growth through mechanisms involving inhibition of mTOR (39). Accordingly, activators of AMPK and inhibitors of mTOR have been shown to account for candidates for chemotherapeutics for tumor growth suppression (37, 40). On the contrary, using the nature of G_1 cells that execute enhanced use of glucose could be another pharmacologic modality. Management of energy status by upregulation of glycolysis in G_1 phase possibly increases cell populations in S and G_2–M phases. As we showed, the cell populations in S and G_2–M phases were only less than 10% *in vivo* (Supplementary Table S1), whereas percentages of the same population become much greater in culture (Fig. 2). These results together with the observation that hypoxia induces G_1 arrest in various cancer cells (41, 42) suggest that a considerable population of cells in the metastatic foci *in vivo* may be under G_1 arrest presumably because of insufficient nutritional states and/or relatively low O_2 concentrations (17). Considering that most of anticancer chemotherapeutic agents target cells in S or G_2–M phases, rendering tumor cells under G_1 phase highly active in glycolysis and proliferative may cause increasing sensitivity to drugs by passing these cells through the metabolic checkpoint to undergo S and G_2–M phases.

Under euglycemic levels of glucose, HCT116 cells also exhibited the above-mentioned metabolic features which were observed under the hyperphysiologic levels (3 g/L glucose). This fact may have a biologic significance that such enhancement of glycolysis could occur in cancer cells under euglycemic environment *in vivo*. Since it has been known that p53 inactivation contributes to glucose consumption by modulating activities of metabolic pathways (43, 44), a question may arise whether such metabolic features could be affected by p53-null. As expected, our results using its isogenic derivative lacking p53 showed that p53 null mutation raised lactate production by 1.5-fold throughout the cell-cycle progression (Fig. 5B). Accordingly, it was likely that a reduction of glycolysis dependence in G_2–M phase of cells lacking p53 is smaller than wild-type cells. Thus, the current finding that transient increase in dependence on oxidative phosphorylation in G_2–M phase and enhancement of glycolysis in G_1 phase may be more obvious with cells carrying wild-type p53 than those lacking p53.

Disclosure of Potential Conflicts of Interest

No potential conflicts of interest were disclosed.

Authors' Contributions

Conception and design: Y. Bao, K. Mukai, M. Suematsu
Development of methodology: T. Hishiki, A. Kubo, M. Ohmura, T. Matsuura, T. Yamamoto, R. Fukuda, M. Suematsu, Y.A. Minamishima
Acquisition of data (provided animals, acquired and managed patients, provided facilities, etc.): Y. Bao, K. Mukai, T. Hishiki, A. Kubo, T. Matsuura, Y. Nagahata, N. Hayakawa, H. Saya
Analysis and interpretation of data (e.g., statistical analysis, biostatistics, computational analysis): Y. Bao, A. Kubo, Y. Sugiura, T. Matsuura, N. Hayakawa, Y.A. Minamishima
Administrative, technical, or material support (i.e., reporting or organizing data, constructing databases): T. Matsuura, M. Suematsu, Y.A. Minamishima
Writing, review, and/or revision of the manuscript: Y. Bao, K. Mukai, M. Suematsu
Study supervision: K. Mukai, M. Suematsu, Y.A. Minamishima

Acknowledgments

The authors thank Drs. A. Miyawaki and A. Sakaue-Sawano (Laboratory for Cell Function and Dynamics, RIKEN, Japan) for the generous gift of Fucci probes. The authors also thank Dr. B. Vogelstein (Johns Hopkins Oncology Center, Baltimore, MD) for the generous gift of HCT116 p53-null cells.

Grant Support

This work was supported by Global COE Program for Human Metabolomics Systems Biology from the Ministry of Education, Culture, Sports, Science and Technology (MEXT), Japan (to M. Suematsu); Research and Development of the Next-Generation Integrated Simulation of Living Matter, a part of the Development and Use of the Next-Generation Supercomputer Project of MEXT (to M. Suematsu); Japan Science and Technology Agency (JST), Exploratory Research for Advanced Technology (ERATO) Suematsu Gas Biology Project (to M. Suematsu); Strategic Research Foundation Grant-aided Project for Private Universities from MEXT (to M. Suematsu); Grant-in-Aid for Research Activity Start-up of Japan Society for the Promotion of Science (to M. Ohmura); Keio University Grant-in-Aid for Encouragement of Young Medical Scientists (to Y. Bao.); and Grant-in-Aid for Scientific Research (type B) of Japan Society for the Promotion of Science (to Y.A. Minamishima).

The costs of publication of this article were defrayed in part by the payment of page charges. This article must therefore be hereby marked *advertisement* in accordance with 18 U.S.C. Section 1734 solely to indicate this fact.

Received November 30, 2012; revised April 23, 2013; accepted May 10, 2013; published OnlineFirst June 5, 2013.

References

1. Warburg O, Posener K, Negelein E. The metabolism of cancer cells. Biochem Zeitschr 1924;152:129–69.
2. Brand KA, Hermfisse U. Aerobic glycolysis by proliferating cells: a protective strategy against reactive oxygen species. FASEB J 1997; 11:388.
3. Tudzarova S, Colombo SL, Stoeber K, Carcamo S, Williams GH, Moncada S. Two ubiquitin ligases, APC/C-Cdh1 and SKP1-CUL1-F (SCF)-beta-TrCP, sequentially regulate glycolysis during the cell cycle. Proc Natl Acad Sci U S A 2011;108:5278–83.
4. Dang CV, Semenza GL. Oncogenic alterations of metabolism. Trends Biochem Sci 1999;24:68–72.
5. Brand K, Aichinger S, Forster S, Kupper S, Neumann B, Nurnberg W, et al. Cell-cycle-related metabolic and enzymatic events in proliferating rat thymocytes. Eur J Biochem 1988;172:695–702.
6. DeBerardinis RJ, Lum JJ, Hatzivassiliou G, Thompson CB. The biology of cancer: metabolic reprogramming fuels cell growth and proliferation. Cell Metab 2008;7:11–20.
7. Vander Heiden MG, Cantley LC, Thompson CB. Understanding the Warburg effect: the metabolic requirements of cell proliferation. Science 2009;324:1029.
8. Wu M, Neilson A, Swift AL, Moran R, Tamagnine J, Parslow D, et al. Multiparameter metabolic analysis reveals a close link between

attenuated mitochondrial bioenergetic function and enhanced glycolysis dependency in human tumor cells. Am J Physiol Cell Physiol 2007;292:C125.
9. Schieke SM, McCoy JP Jr, Finkel T. Coordination of mitochondrial bioenergetics with G_1 phase cell cycle progression. Cell Cycle 2008;7:1782–7.
10. Sweet S, Singh G. Accumulation of human promyelocytic leukemic (HL-60) cells at two energetic cell cycle checkpoints. Cancer Res 1995;55:5164–7.
11. Schulz TJ, Thierbach R, Voigt A, Drewes G, Mietzner B, Steinberg P, et al. Induction of oxidative metabolism by mitochondrial frataxin inhibits cancer growth: Otto Warburg revisited. J Biol Chem 2006;281:977–81.
12. van den Bogert C, van Kernebeek G, de Leij L, Kroon AM. Inhibition of mitochondrial protein synthesis leads to proliferation arrest in the G_1 -phase of the cell cycle. Cancer Lett 1986;32:41–51.
13. Mitra K, Wunder C, Roysam B, Lin G, Lippincott-Schwartz J. A hyperfused mitochondrial state achieved at G_1–S regulates cyclin E buildup and entry into S phase. Proc Natl Acad Sci U S A 2009;106:11960–5.
14. Rajput A, Dominguez San Martin I, Rose R, Beko A, Levea C, Sharratt E, et al. Characterization of HCT116 human colon cancer cells in an orthotopic model. J Surg Res 2008;147:276–81.
15. Ishizu K, Sunose N, Yamazaki K, Tsuruo T, Sadahiro S, Makuuchi H, et al. Development and characterization of a model of liver metastasis using human colon cancer HCT-116 cells. Biol Pharm Bull 2007;30:1779–83.
16. Gavert N, Sheffer M, Raveh S, Spaderna S, Shtutman M, Brabletz T, et al. Expression of L1-CAM and ADAM10 in human colon cancer cells induces metastasis. Cancer Res 2007;67:7703–12.
17. Handa K, Ohmura M, Nishime C, Hishiki T, Nagahata Y, Kawai K, et al. Phosphorescence-assisted microvascular O(2) measurements reveal alterations of oxygen demand in human metastatic colon cancer in the liver of superimmunodeficient NOG mice. Adv Exp Med Biol 2010;662:423–9.
18. Ito M, Hiramatsu H, Kobayashi K, Suzue K, Kawahata M, Hioki K, et al. NOD/SCID/gamma(c)(null) mouse: an excellent recipient mouse model for engraftment of human cells. Blood 2002;100:3175–82.
19. Sakaue-Sawano A, Kurokawa H, Morimura T, Hanyu A, Hama H, Osawa H, et al. Visualizing spatiotemporal dynamics of multicellular cell-cycle progression. Cell 2008;132:487–98.
20. Hattori K, Kajimura M, Hishiki T, Nakanishi T, Kubo A, Nagahata Y, et al. Paradoxical ATP elevation in ischemic penumbra revealed by quantitative imaging mass spectrometry. Antioxid Redox Signal 2010;13:1157–67.
21. Monton MR, Soga T. Metabolome analysis by capillary electrophoresis-mass spectrometry. J Chromatogr A 2007;1168:237–46.
22. Soga T, Ohashi Y, Ueno Y, Naraoka H, Tomita M, Nishioka T. Quantitative metabolome analysis using capillary electrophoresis mass spectrometry. J Proteome Res 2003;2:488–94.
23. Shintani T, Iwabuchi T, Soga T, Kato Y, Yamamoto T, Takano N, et al. Cystathionine beta-synthase as a carbon monoxide-sensitive regulator of bile excretion. Hepatology 2009;49:141–50.
24. Kinoshita A, Tsukada K, Soga T, Hishiki T, Ueno Y, Nakayama Y, et al. Roles of hemoglobin Allostery in hypoxia-induced metabolic alterations in erythrocytes: simulation and its verification by metabolome analysis. J Biol Chem 2007;282:10731–41.
25. Miyoshi H, Blomer U, Takahashi M, Gage FH, Verma IM. Development of a self-inactivating lentivirus vector. J Virol 1998;72:8150–7.
26. Miyoshi H, Takahashi M, Gage FH, Verma IM. Stable and efficient gene transfer into the retina using an HIV-based lentiviral vector. Proc Natl Acad Sci U S A 1997;94:10319–23.
27. Kubo A, Ohmura M, Wakui M, Harada T, Kajihara S, Ogawa K, et al. Semi-quantitative analyses of metabolic systems of human colon cancer metastatic xenografts in livers of superimmunodeficient NOG mice. Anal Bioanal Chem 2011;400:1895–904.
28. Hayasaka T, Goto-Inoue N, Ushijima M, Yao I, Yuba-Kubo A, Wakui M, et al. Development of imaging mass spectrometry (IMS) dataset extractor software, IMS convolution. Anal Bioanal Chem 2011;401:183–93.
29. Rebrin I, Kamzalov S, Sohal RS. Effects of age and caloric restriction on glutathione redox state in mice. Free Radic Biol Med 2003;35:626–35.
30. Greiner EF, Guppy M, Brand K. Glucose is essential for proliferation and the glycolytic enzyme induction that provokes a transition to glycolytic energy production. J Biol Chem 1994;269:31484–90.
31. Singh P, Salih M, Leddy JJ, Tuana BS. The muscle-specific calmodulin-dependent protein kinase assembles with the glycolytic enzyme complex at the sarcoplasmic reticulum and modulates the activity of glyceraldehyde-3-phosphate dehydrogenase in a Ca2+/calmodulin-dependent manner. J Biol Chem 2004;279:35176–82.
32. Zhang H, Gao P, Fukuda R, Kumar G, Krishnamachary B, Zeller KI, et al. HIF-1 inhibits mitochondrial biogenesis and cellular respiration in VHL-deficient renal cell carcinoma by repression of C-MYC activity. Cancer Cell 2007;11:407–20.
33. Chen Z, Odstrcil EA, Tu BP, McKnight SL. Restriction of DNA replication to the reductive phase of the metabolic cycle protects genome integrity. Science 2007;316:1916–9.
34. Eigenbrodt E, Reinacher M, Scheefers-Borchel U, Scheefers H, Friis R. Double role for pyruvate kinase type M2 in the expansion of phosphometabolite pools found in tumor cells. Crit Rev Oncog 1992;3:91–115.
35. Shchipakin VN, Evtodienko YV. Glycolytic intermediate levels in the cell-cycle of sea-urchin eggs and bacteria. Comp Biochem Physiol B Biochem Mol Biol 1984;77:245–7.
36. Jones RG, Plas DR, Kubek S, Buzzai M, Mu J, Xu Y, et al. AMP-activated protein kinase induces a p53-dependent metabolic checkpoint. Mol Cell 2005;18:283–93.
37. Shaw RJ. Glucose metabolism and cancer. Curr Opin Cell Biol 2006;18:598–608.
38. Slawson C, Copeland RJ, Hart GW. O-GlcNAc signaling: a metabolic link between diabetes and cancer? Trends Biochem Sci 2010;35:547–55.
39. Gwinn DM, Shackelford DB, Egan DF, Mihaylova MM, Mery A, Vasquez DS, et al. AMPK phosphorylation of raptor mediates a metabolic checkpoint. Mol Cell 2008;30:214–26.
40. Tennant DA, Duran RV, Gottlieb E. Targeting metabolic transformation for cancer therapy. Nat Rev Cancer 2010;10:267–77.
41. Box AH, Demetrick DJ. Cell cycle kinase inhibitor expression and hypoxia-induced cell cycle arrest in human cancer cell lines. Carcinogenesis 2004;25:2325–35.
42. Semenza GL. Hypoxia. Cross talk between oxygen sensing and the cell cycle machinery. Am J Physiol Cell Physiol 2011;301:C550–2.
43. Vousden KH, Ryan KM. p53 and metabolism. Nat Rev Cancer 2009;9:691–700.
44. Jiang P, Du W, Wang X, Mancuso A, Gao X, Wu M, et al. p53 regulates biosynthesis through direct inactivation of glucose-6-phosphate dehydrogenase. Nat Cell Biol 2011;13:310–6.